A Nonlinear Lumped Equivalent Circuit Model for a Single Uncollapsed Square CMUT Cell

Mohammad Maadi, *Student Member, IEEE*, and Roger J. Zemp, *Member, IEEE*

***Abstract*— An accurate nonlinear lumped equivalent circuit model is used for modeling of capacitive micromachined ultrasonic transducers (CMUTs). Finite-element analysis (FEA) is a powerful tool for the analysis of CMUT arrays with a small number of cells while with the harmonic balance (HB) analysis of the lumped equivalent circuit model, the entire behavior of a large-scale arbitrary CMUT array can be modeled in a very short time. Recently, an accurate nonlinear equivalent circuit model for uncollapsed single circular CMUT cells has been developed. However, the need for an accurate large-signal circuit model for CMUT cells with square membranes motivated us to produce a new nonlinear large-signal equivalent circuit model for uncollapsed CMUT cells. In this paper, using analytical calculations and FEA as the tuning tool, a precise large signal equivalent circuit model of square CMUT dynamics was developed and showed excellent agreement with finite-element modeling (FEM) results. Then, different CMUT single cells with square and circular membranes were fabricated using a standard sacrificial release process. Model predictions of resonance frequencies and displacements closely matched experimental vibrometer measurements. The framework presented here may prove valuable for future design and modeling of CMUT arrays with square membranes for ultrasound imaging and therapy applications.**

***Index Terms*— Capacitive micromachined ultrasonic transducers (CMUTs), microelectromechanical systems (MEMSs), microfabrication, nonlinear lumped equivalent circuit model.**

I. Introduction

CAPACITIVE micromachined ultrasonic transducers (CMUTs) have attracted considerable attention in the ultrasound community owing to their potential for mass fabrication and cointegration with electronics [1]–[6]. In addition, recent efforts have focused on applications not easily addressed with conventional piezoelectric materials, including bias-switchable crossed-electrode 2-D arrays [7] and multifrequency interlaced transducers for acoustic [8]–[11] and photoacoustic imaging applications [12]. Electromechanical modeling of these devices will be critical for optimizing the performance of the arrays.

Manuscript received December 14, 2018; accepted April 29, 2019. Date of publication May 3, 2019; date of current version August 1, 2019. This work was supported in part by the Natural Sciences and Engineering Research Council of Canada under Grant CHRPJ 462510 and Grant RGPIN 355544 Zemp, in part by the Alberta Innovates Technology Futures, in part by nanoBridge, in part by Mitacs under Grant MI MEPF IT04591, and in part by the Canadian Institutes of Health Research under Grant CPG 134739. *(Corresponding author: Mohammad Maadi.)*

The authors are with the Electrical and Computer Engineering Department, University of Alberta, Edmonton, AB T6G 2R3, Canada (e-mail: maadi@ualberta.ca; rzemp@ualberta.ca).

Digital Object Identifier 10.1109/TUFFC.2019.2914608

Much of the previous modeling literature, which is based on Mason's equivalent circuit [13], has focused on circular membranes owing to simplifications associated with cylindrical symmetry [14]–[16]. In these cases, equivalent-circuit models have proven to be computationally superior over finite-element modeling (FEM) with excellent accuracy. However, finite-element analysis (FEA) is still a powerful tool to predict the nonlinear effects of the CMUT and higher order harmonics.

Square membrane CMUTs have been widely used and make better use of active wafer real estate compared to circular membranes. Their modeling, however, is more complex [17], and most prior work has relied on FEA, which is time-consuming and practically intractable for large arrays. Although static deflection models have been previously presented for square membranes [18]–[21], dynamic lumped equivalent circuit models have only been developed for the small signal regime [17], where important nonlinear behavior is ignored. The Degertekin group developed a 2-D finite-element hybrid model [22], [23], which is computationally advantageous over the full 3-D model; however, the computational burden is still nontrivial and the lack of an equivalent circuit model makes cosimulation with electronics difficult.

In this paper, a large-signal nonlinear equivalent circuit model is developed for single CMUT cells with square membranes by obtaining new circuit parameters for the model developed in [14]. First, we studied the deflection profile of the square membranes using static FEA and analytical calculations. Then, the nonlinear capacitance of the CMUT was obtained relative to the normalized deflection of the membrane. Using the root mean square (rms) of the plate displacement and velocity, the electrostatic force acting on the membrane was found and compared with circular plates. The membrane rms compliance was found for thin and thick plates and all obtained parameters were implemented in a circuit model. The nonlinear equivalent circuit model is based on accurate approximations of membrane deflection and velocity profiles as well as self-radiation impedance, for which there are no known analytical closed-form solutions [17]. The model is implemented in the commercial circuit simulator Advanced Design System Environment (Agilent Technologies Inc., Santa Rosa, CA, USA).

Model predictions of the membrane static deflections for different dc biases, membrane dynamic displacement amplitude and phase, resonance frequency, and total electrical

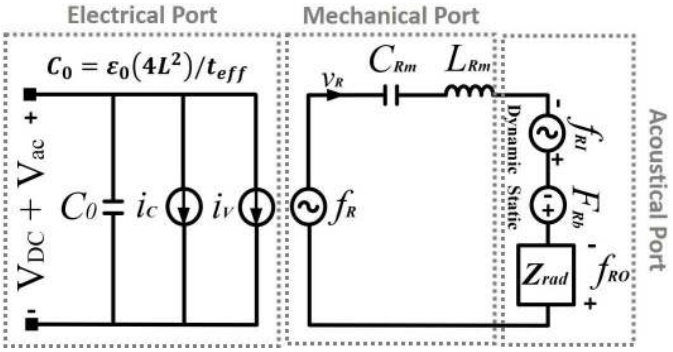

Fig. 1. Nonlinear large signal equivalent circuit model of a CMUT with square membrane.

conductance closely matched the 3-D FEM analysis for various single square CMUT cells with thin and thick membranes. Then, the results were compared with circular CMUT cells when the half-side length of the square CMUT is assumed to be equal to the radii of the circular cell. It will be shown that there is a considerable difference between the simulation results of the counterpart circular and square CMUT cells. The fabricated single transducers using a standard sacrificial release process are then compared with circuit simulation results. The predictions for resonance frequencies and displacements show a good agreement with experimental vibrometer measurement results in air.

Although some have used circular CMUT models as an approximation to square membrane models, our paper aims to show some important differences that may make a difference when designing next-generation transducers with maximal real estate for photoacoustic and ultrasound imaging-therapy applications.

II. Nonlinear Lumped Equivalent Circuit Model for a Single Square CMUT Cell

We based our large signal equivalent circuit on the model developed in [14] in which the model parameters are provided for single CMUT devices with circular membranes. However, by considering the same circuit, different circuit parameters are used for the CMUTs with square membranes. The circuit model consists of three interacting physical domains of a CMUT including electrical, mechanical, and acoustical ports (Fig. 1).

A. Deflection Profile

Fig. 2 shows the basic top and cross-sectional views of a circular and square CMUT cells with an applied voltage. The general form of a square CMUT deflection profile with side length of 2L can be written as [20]

$$D(x,y,t) = x_p(t)\left[1-\left(\frac{x}{L}\right)^2\right]^2\left[1-\left(\frac{y}{L}\right)^2\right]^2\sum_{n=0}^{N} C_n\left[\left(\frac{x}{L}\right)^2+\left(\frac{y}{L}\right)^2\right]^n \quad (1)$$

where L is the half-side length of the aperture, x and y are the distances across the plate in two directions, x_p is the displacement at the center of the membrane, and C_n coefficients can be adjusted for any design parameters and are determined by FEA.

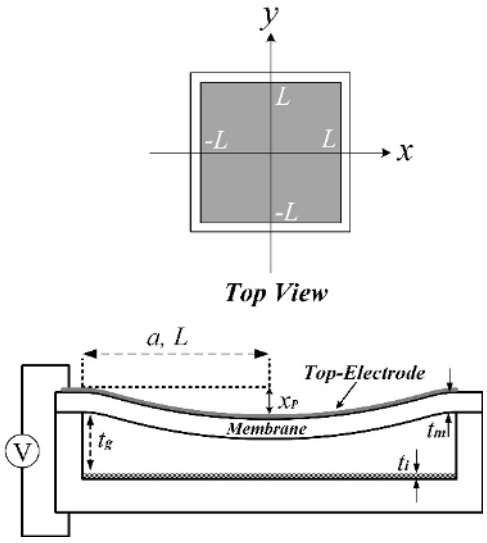

Fig. 2. Top and cross-sectional view of the CMUT geometry with applied voltage and dimensional parameters.

Since the analytical deflection calculations for the plates with square membranes are complicated, approximate methods must be used to solve the plate equation. Rahman *et al.* [20] provided a deflection profile for square CMUTs with a membrane thickness of 0.5–3 μm and half-side length of 100–500 μm. However, the provided expression loses accuracy while the membrane size shrinks to smaller values ($L < 100$ μm). As will be shown later, the CMUT membranes can be considered as thin ($L/t_m \geq 15$) or thick ($L/t_m < 15$) plates. First, the model parameters are achieved by considering the thin plate condition. Then using FEA, the model will be expanded for thick membranes by applying the obtained correction factors to the compliance of the membrane. The approximate deflection profile of a CMUT with a square membrane can be written as

$$D(x,y,t) = x_p(t)\left[1-\left(\frac{x}{L}\right)^2\right]^2\left[1-\left(\frac{y}{L}\right)^2\right]^2\left[1+\beta\left\{\left(\frac{x}{L}\right)^2+\left(\frac{y}{L}\right)^2\right\}\right] \quad (2)$$

which is a special case of (1) for $N = 2$. Thomsen *et al.* [18] found the coefficient β for the plates on a silicon (001) substrate and aligned to the [110] direction as

$$\beta = \frac{182 + 143k_2}{1432 + 91k_2} \quad (3)$$

where k_2 is the plate coefficient and $\beta_{\text{low}} = 0.23920$ and $\beta_{\text{high}} = 0.23691$ are obtained for single-crystal silicon with low ($150\ \Omega - \text{cm}, \sim 2.8 \times 10^{13}\ \text{cm}^{-3}$) and high doping ($3.26\ \text{m}\Omega - \text{cm}, \sim 2.1 \times 10^{19}\ \text{cm}^{-3}$), respectively, as defined in [17]. We use $\beta = 0.23691$ in our simulations and found that this provides a reasonable agreement with FEM for a wide range of thin membranes with different materials including

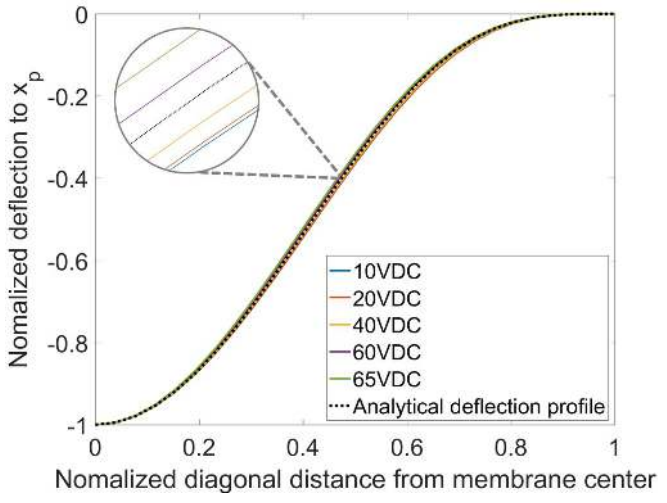

Fig. 3. Comparison of FEA deflection profile of 1-μm silicon nitride diaphragm with the approximate analytical solution, plotted from the center to the edge of the plate. $L = 20$ μm and $t_m = 1$ μm. The silicon nitride membrane parameters are provided in [10, Table IV].

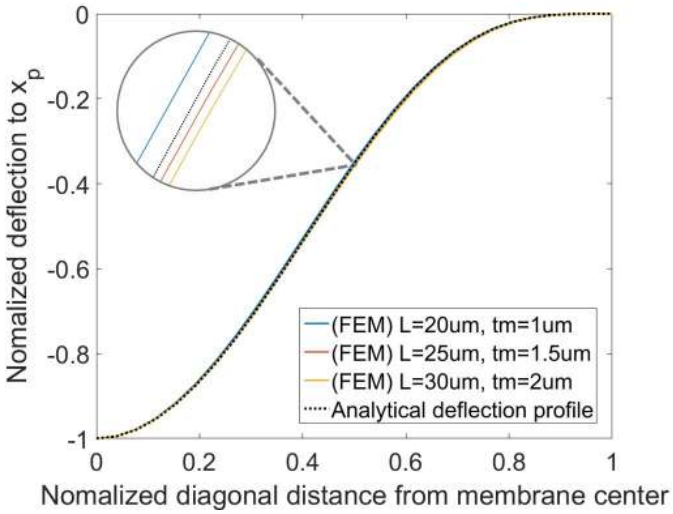

Fig. 4. Comparison of FEA deflection profile of different silicon nitride membranes with the approximate analytical solution, plotted from the center to the edge of the plate. $V_{\text{dc}} = 60$ V.

silicon nitride which we are mostly interested in. Fig. 3 shows the normalized deflection profile, $D(x, y)/x_p$, of a target thin silicon nitride square membrane ($L = 20$ μm, $t_m = 1$ μm) versus the normalized diagonal distance from the center of the plate for different biasing voltages in water immersion.

The applied dc voltage is increased until the membrane collapsed at 69 V. The normalized deflection profile is slightly changed under different bias voltages. However, the approximate analytical solution using $\beta_{\text{high}} = 0.23691$ gives us an acceptable deflection profile to start obtaining the nonlinear lumped equivalent circuit parameters of a square CMUT cell. The membrane material parameters of the membrane can be found in [10, Table IV]. For further investigation, the similar analysis was accomplished for different types of thin membranes with different sizes and thicknesses with 60-V dc bias (Fig. 4). The collapse voltages for considered three different designs from top to bottom are 69, 82, and 87 V and the applied 60-V bias is 87%, 73%, and 69% of their collapse voltages, respectively.

B. Capacitance

The capacitance, $\delta C(x, y, t)$, of a concentric narrow square on the membrane with dimension of dx by dy can be expressed as

$$\delta C(x, y, t) = \frac{\varepsilon_0 dx dy}{t_{ge} - D(x, y, t)} \tag{4}$$

where $\varepsilon_0 = 8.85 \times 10^{-12}$ F/m is the permittivity of the gap in free space and $t_{ge} = t_g + t_i/\varepsilon_r$ is the effective gap height in which ε_r is the relative permittivity of the insulating material, t_g is the thicknesses of the vacuum gap height, and t_i determines the insulating layer thickness.

The total capacitance, $C(t)$, of the deflected membrane with full electrode can be written as

$$C(t) = \frac{1}{t_{ge}} \int_{-L}^{L} \int_{-L}^{L} \frac{\varepsilon_0}{1 - \frac{1}{t_{ge}} D(x, y, t)} dx dy. \tag{5}$$

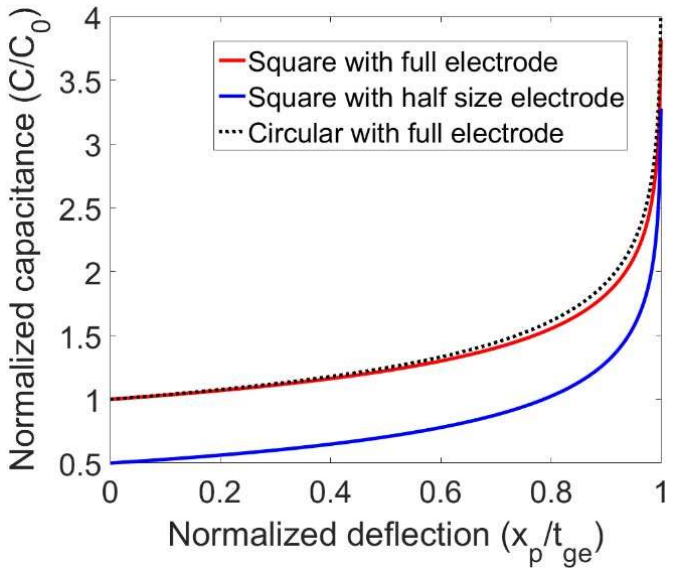

Fig. 5. Comparison of normalized total capacitance versus normalized membrane deflection for a circular plate with full electrode and a square membrane with full- and concentric half-size electrodes.

However, the capacitance can be found for the membranes with a partial electrode of inner half-side length of L_i and outer half-side length of L_o. Since there is no analytical solution for the capacitance calculation of the square CMUTs, the integration is performed numerically. Fig. 5 shows the analytical solution for a circular membrane with full electrode [14, eq. (2)] and numerical solutions for the capacitance of a square plate with full- and concentric half-size electrodes. Note that for the plates with half-size concentric electrodes, the area of the electrode is $2L^2$ and the intervals of the integral in (5) will be from $-\sqrt{2}\ L/2$ to $\sqrt{2}\ L/2$.

The total capacitance of the deflected membrane with full-area electrodes can be expressed as

$$C(t) = C_0 g\left(\frac{x_p(t)}{t_{ge}}\right) = C_0 g(u) \tag{6}$$

where $C_0 = \varepsilon_0 4L^2/t_{ge}$ is the capacitance at zero deflection, and the function $g(u)$, which describes the shape of the capacitance curve, can be found by performing the higher order polynomial fitting to the numerically obtained solution for three different deflection ranges: 1) low deflection $0 < u < 1e-3$; 2) the range below the pull-in distance $1e-3 < u < 0.5$; and 3) the range beyond the pull-in distance of $0.5 < u < 0.99$. Note that [17, eq. 82] calculates the normalized pull-in distance as 0.466 without additional pressure loading, which we are rounding to 0.5. Fig. 6 demonstrates the numerically obtained solutions for the normalized capacitance of a square plate and its first and second derivatives for three different normalized deflection ranges. The goodness of fitting on obtained graphs is increased dramatically when the polynomial fitting is done separately for divided membrane deflection ranges. The polynomial coefficients of (7) are provided in Table V of the Appendix

$$g(u) = \sum_{n=0}^{9} a_n u^n. \tag{7}$$

Note that for negative values of peak displacement ($x_p(t) < 0$), $g(u)$ will be replaced by $g(-u)$, which is a useful expression for circuit simulators.

C. RMS, Average, and Peak Displacement and Velocity Coefficients

Since the average displacement and velocity measurements are problematic in some cases, the rms velocity distribution on the membrane surface, v_{rms}, is preferred instead of the average velocity, v_{ave}, as the lumped variable at the mechanical side of the circuit [15]. For instance, higher harmonic deflection profiles may generate zero average displacement and velocity. In this case, the mechanical radiation impedance will go to infinity and makes the mechanical port of the lumped model open circuit. This problem can be handled by defining the rms displacement of the square membrane profile as

$$\begin{aligned} x_R(t) &= \sqrt{\frac{1}{4L^2}\int_{-L}^{L}\int_{-L}^{L} D^2(x,y,t)dxdy} \\ &= x_p(t)\sqrt{\frac{16384(92\beta^2+572\beta+1573)}{156080925}} \end{aligned} \tag{8}$$

and the average displacement, $x_A(t)$, for the membrane displacement profile given by (1) is

$$x_A(t) = \frac{1}{4L^2}\int_{-L}^{L}\int_{-L}^{L} D(x,y,t)dxdy = x_p(t)\left[\frac{64(2\beta+7)}{1575}\right]. \tag{9}$$

Table I summarizes the displacement rms and average coefficients for low and high doping cases. Note that the rms and average displacements, $x_R(t)$ and $x_A(t)$, for the circular membranes are $x_p(t)/\sqrt{5} = 0.4472x_p(t)$ and $x_p(t)/3 = 0.3333x_p(t)$, respectively [14]. For the rest of this paper, we will consider $Coeff_{RMS}$ and $Coeff_{AVG}$ as the membrane rms and average coefficients, respectively (Table I).

TABLE I
DISPLACEMENT RMS AND AVERAGE COEFFICIENTS FOR THE SQUARE PLATES

β	$x_R(t)$	$x_A(t)$
$\beta_{low} = 0.23691$	$0.42413x_P(t)$	$0.3037x_P(t)$
$\beta_{High} = 0.23920$	$0.42430x_P(t)$	$0.3039x_P(t)$
$x_R(t) = Coeff_{RMS} \times x_P(t)$		
$x_A(t) = Coeff_{AVG} \times x_P(t)$		

According to $v(t) = dx(t)/dt$, the membrane velocity has the same rms and average coefficients as shown for the plate displacement in Table I.

The electrostatic force acting on the small square area $dxdy$ is calculated by taking the derivative of the stored energy in the capacitance with square plates, while the CMUT is driven by the combination of dc and ac voltages. The rms force, $f_R(t)$, is given by [14, eq. (6)]

$$f_R(t) = \frac{\partial E(t)}{\partial x_R(t)} \tag{10}$$

where $E(t) = 1/2C(t)V^2(t)$ is the instantaneous energy stored on the capacitance, if $V(t)$ is applied as the voltage across the capacitance. Then, the rms force can be written as [14, eq. (7)]

$$\begin{aligned} f_R(t) &= \frac{V^2(t)}{2}\frac{\partial C(t)}{\partial x_R(t)} \\ &= \left(\frac{1}{Coeff_{RMS}}\right)\frac{C_0V^2(t)}{2t_{ge}}g'(u). \end{aligned} \tag{11}$$

For the CMUTs with full electrodes, Fig. 7 depicts the comparison of rms electrostatic force normalized with $C_0V^2(t)/4t_{ge}$ for devices with circular and square membranes.

D. Compliance and Mass of the Square Membrane

The accuracy of the proposed model depends on the agreement between the parameters of the equivalent circuit model and the actual device parameters. For some of the parameters including the membrane deflection and velocity profiles, we are not able to use the exact form, and for some calculations such as capacitance and mechanical radiation impedance, there are no precise analytical solutions, hence we need to perform numerical calculations or use approximations. Since the device resonance frequency and the snap-down voltage depend on the compliance of the membrane, C_m, and the compliance is related to the membrane physical dimensions (softer compliance for thicker plates), the relationship between the compliance and membrane physical dimensions needs to be adequately modeled to compensate the initial thin plate approximation and keeps the accuracy of the equivalent circuit for thicker plates.

Yamaner *et al.* [24, eq. (1)] used FEM simulation results to develop a correction factor for thick circular plates, applied to the rms compliance of a circular membrane. Using the same approach, the accuracy of the model is increased by applying

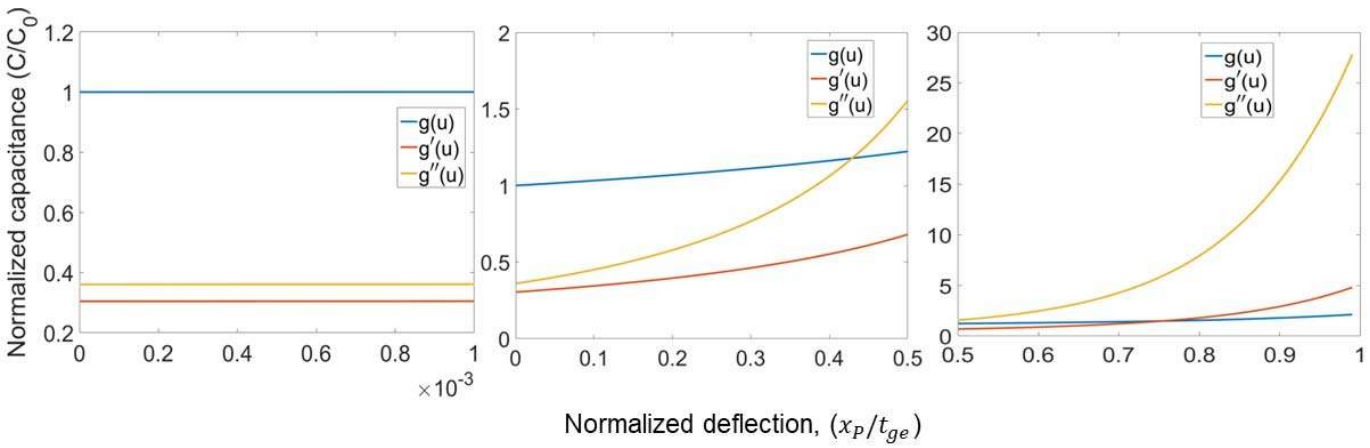

Fig. 6. Normalized capacitance of a square plate and its derivatives for normalized deflection of $0 < (x_p/t_{ge}) < 1e-3$ (left), $1e-3 < (\frac{x_p}{t_{ge}}) < 0.5$ (middle), and $0.5 < (x_p/t_{ge}) < 0.99$ (right).

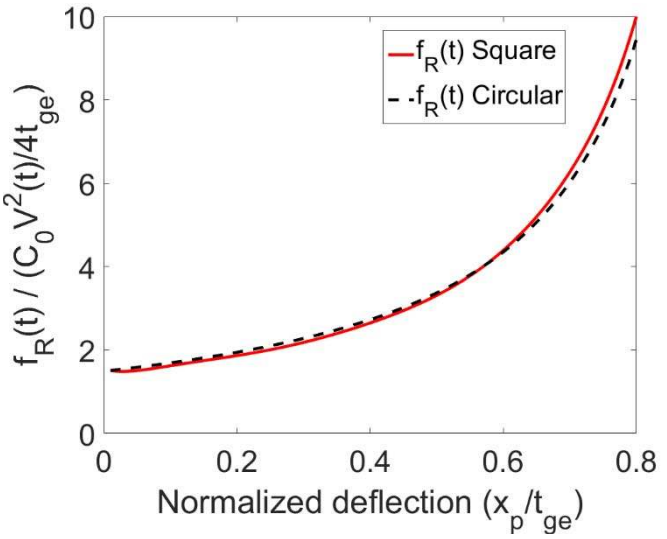

Fig. 7. Comparison of rms normalized electrostatic force as a function of normalized membrane deflection.

different correction factors separately for thin and thick square membranes.

For the structure shown in Fig. 2, the flexural rigidity of the square plate is given by [17, eq. (2)]

$$D = \frac{Y_0 t_m^3}{12(1-\sigma^2)} \tag{12}$$

where Y_0 is Young's modulus, t_m is the thickness of the membrane, and σ is the Poisson ratio. The linear spring constant of the square membrane is [17]

$$K_S = \frac{768D}{L^2} \tag{13}$$

with compliance given as $C_m = 1/K_S$. As explained in [14], the capacitance in Mason's circuit representing the compliance of the plate needs to be multiplied by $|v_{\text{rms}}|^2/|v_{\text{avg}}|^2$ to preserve the resonance frequency in vacuum. Then, the rms value of the compliance for devices with square membranes can be written as [24, eq. (7)]

$$C_{Rm} = \left(\frac{Coeff_{RMS}}{Coeff_{AVG}}\right)^2 \frac{(1-\sigma^2)L^2}{64 Y_0 t_m^3} \tag{14}$$

TABLE II
COEFFICIENTS OF THE COMPLIANCE CORRECTION FACTOR EQUATION FOR THIN AND THICK MEMBRANES

Membrane	a	b	c
Thin	1.10628	0.00597	−0.76604
Thick	1.10628	5.305	2.08

where $Coeff_{RMS}$ and $Coeff_{AVG}$ are given in Table I.

We previously showed excellent agreement between FEM and equivalent circuit model for circular CMUTs in [10]. The circuit parameters for thin circular membranes are obtained using exact analytical calculations, but for thin square membranes, we used approximate deflection profile and numerical calculations to find the nonlinear capacitance of the device. To obtain good agreements between FEM, model, and experiments, two correction factors are obtained by ANSYS 3-D FEA for thin ($L/t_m > 15$) and thick ($L/t_m < 15$) membranes and then applied to C_{Rm} separately as [26]

$$C'_{Rm} = C_{Rm}\left[a + b\left(\frac{t_m}{L}\right)^c\right] \tag{15}$$

with provided coefficients in Table II.

In the proposed circuit model shown in Fig. 1, the inductance corresponds to the total mass of the membrane and the rms value is

$$L_{Rm} = \rho(4L^2)t_m \tag{16}$$

where ρ is the density of the membrane.

It is necessary to consider the effects of the self-acoustic radiation impedance on the behavior of the CMUT, especially for immersion media. The radiation impedance, Z, of a radiator is determined by dividing the total radiated power, P, from the transducer by the square of the absolute value of an arbitrary nonzero reference velocity, V [25]. The self-radiation impedance of a flexural circular clamped disk located on an infinite rigid baffle is given in [10, eq. (36)] and [15]. The same expression may be used as an approximation for a

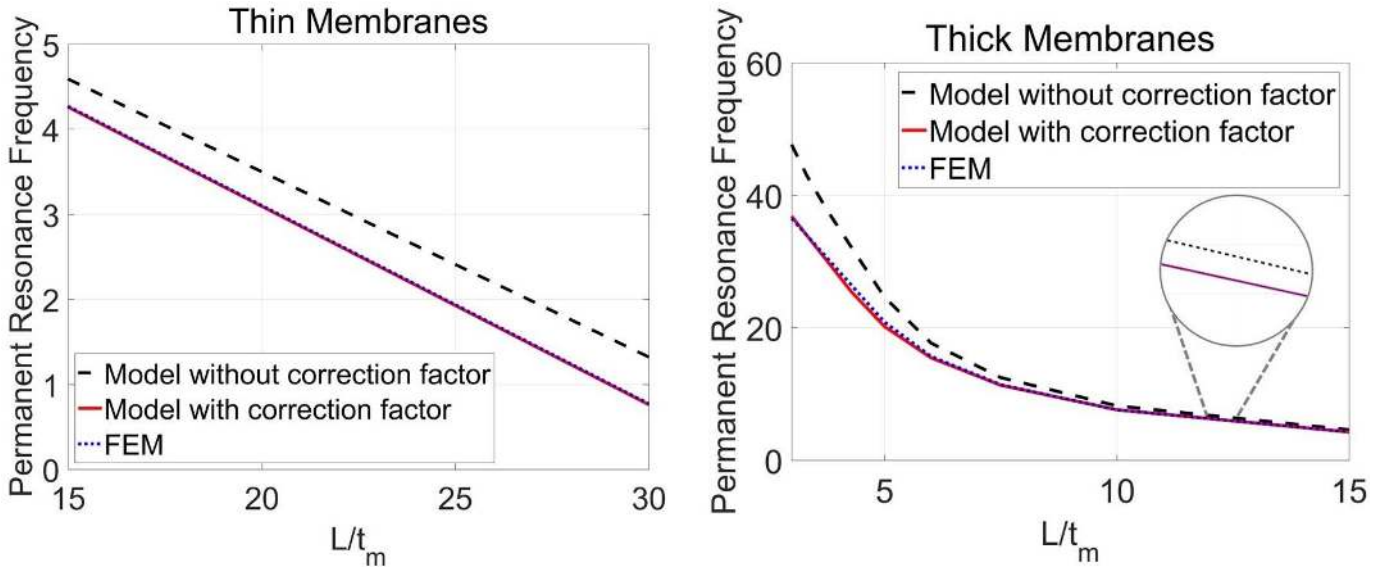

Fig. 8. Comparison of FEM with circuit simulation results for permanent resonance frequency of thin and thick plates in water immersion with and without applying the correction factors to the compliance of the membrane. The half-side length of the device is 30 μm, the thickness of the membrane is swept from 1 to 10 μm, and a dc bias of 30 V is applied. Device parameters are provided in [10, Table IV].

square clamped radiator by replacing the area of the circular plate (πa^2) with the area of a square disk ($4L^2$). The self-radiation impedance is implemented in the acoustical port of the circuit model. The choice to use the square area $4L^2$ rather than the circular area πa^2 in the expression for the self-radiation impedance was purely phenomenological and based on model accuracy compared to FEM simulations. This reflects slightly more moving membrane real estate in the square membrane case compared to the circular membrane case.

The accuracy of the model in static and dynamic conditions is tested for thin and thick plates by comparing the FEM and circuit simulation results for different designs. ANSYS 3-D axisymmetric models of CMUTs with quarter periodic sections are utilized by applying the rigid boundary conditions. More details about the finite-element simulations for transducers with circular membranes are provided in [26] as we used the similar method to model and simulate the CMUTs with square membranes. The CMUT is clamped from the side lengths and considered as a clamped radiator. Fig. 8 shows the comparison of finite-element simulations with the results obtained by the circuit model with and without applying the correction factors for the permanent resonance frequency of thin and thick plates in water immersion. The permanent resonance frequency of the CMUT is defined as the frequency of the peak total conductance G (the real part of the admittance) [10], [14]. The parameters of [10, Table IV] are used for simulations, except the dc voltage applied is 30 V, the half-side length of the CMUT is considered 30 μm and the thickness of the membrane is swept from 1 to 10 μm. The dynamic simulation results show good agreement with FEM simulations for both thin and thick plates.

More investigation is done by testing the accuracy of the model in static conditions for two thick plates ($L = 93$ μm with 7 and 14 μm thicknesses) by comparing the static deflection obtained by finite-element simulations and circuit models for different dc biases in water immersion. As shown in Fig. 9, the model can predict the peak static deflection values of a target CMUT cell under different dc biases.

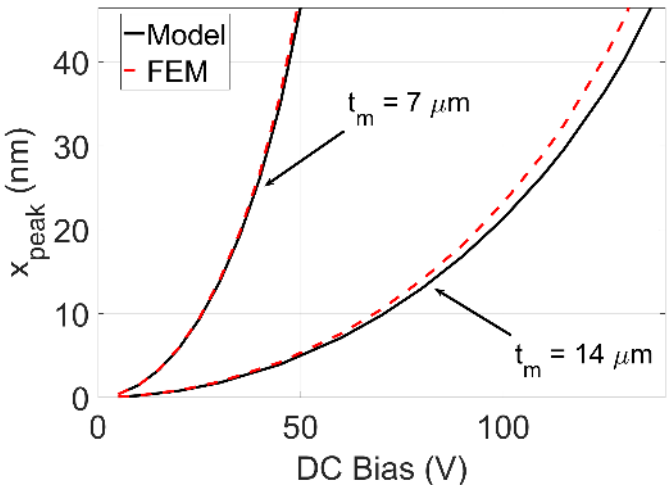

Fig. 9. Comparison of peak static deflections of a square CMUT cell with a half-side length of 93 μm for two thick membranes obtained by FEM and lumped equivalent circuit model using parameters of [10, Table IV] in water immersion.

Fig. 10 demonstrates the error of the equivalent circuit model simulations for peak displacements compared to FEM for two different designs shown in Fig. 9. It is obvious to see that the model is more accurate for thinner membranes, which is more desirable for our fabrication purposes. For example, if we bias the considered CMUT cells with 75% of their collapse voltages, the accuracy of the model is more than 97% and 91% for the designs with the thicknesses of 7 and 14 μm, respectively.

III. Comparison with FEM Analysis

In Section II, the dc performance of the harmonic balance (HB) circuit model was compared with the finite-element static analysis results. Moreover, the large signal electrical

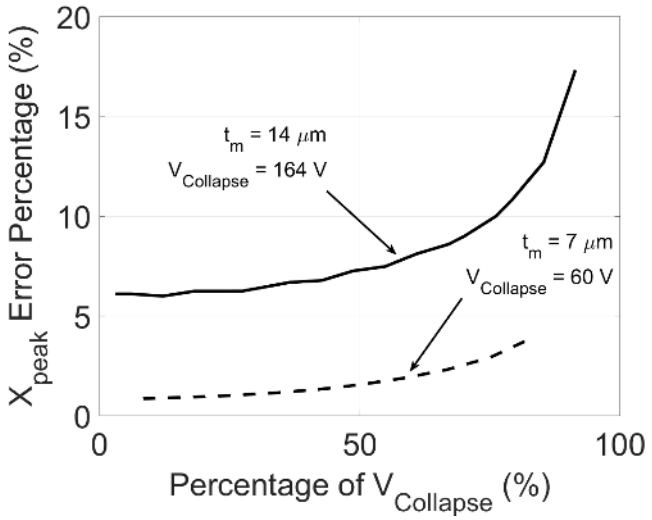

Fig. 10. Error analysis of the peak displacement calculations for two different designs shown in Fig. 9. The graph shows the accuracy of the proposed equivalent circuit model compared to FEM.

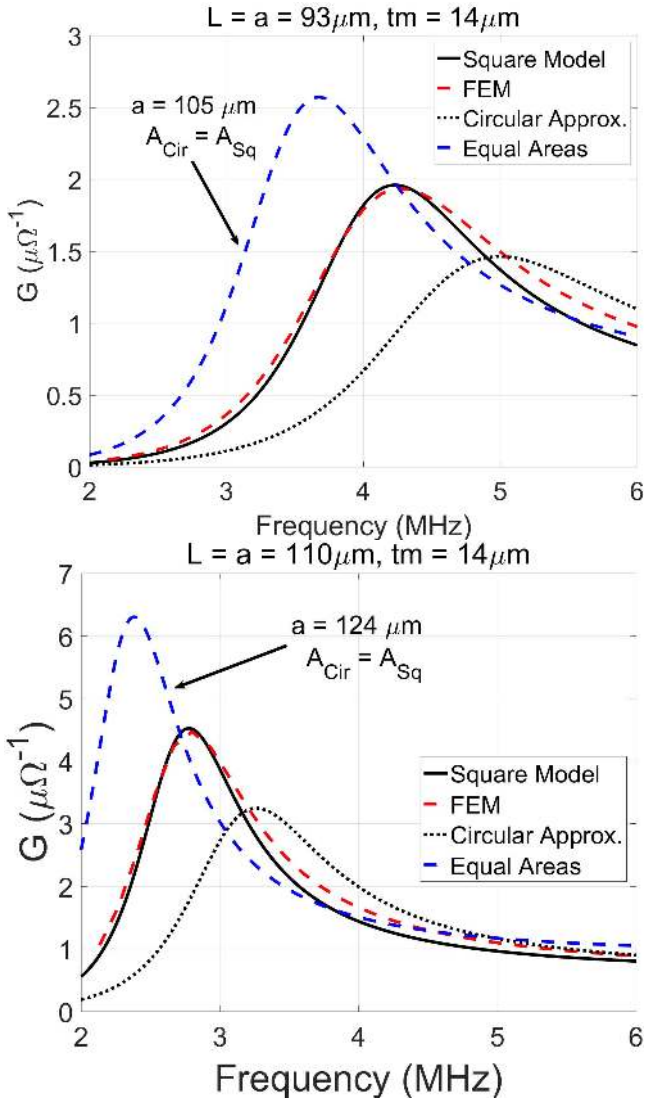

Fig. 11. Comparison of total electrical conductance for square and circular CMUT cells with provided parameters in [10, Table IV] when the half-side length of the square CMUT is assumed to be equal to the radii of the circular membrane and when the circular and square disks have the same areas.

conductance of a square CMUT with different design parameters was simulated and compared with FEM. All the circuit simulations were done in water immersion and obtained results were in excellent agreement with FEA. In this section, we will do more dynamic simulations using different CMUT parameters provided in [10, Table IV] and compare with FEM results.

The large signal HB circuit model obtained in [14] and [15] for circular CMUT cells may be used as an approximation to model the CMUTs with square membranes by assuming that the half-side length of the square plate is equal to the radii of the circular membrane. Fig. 11 demonstrates the total electrical conductance of two circular and square CMUTs with different membrane sizes, 93 and 110 μm. Using the parameters provided in [10, Table IV], the square CMUTs are modeled in FEM and compared with the circuit simulation results for circular and square devices. As shown, the circuit model with proposed parameters for square CMUTs matches the 3-D FEA, while the circular approximation does not provide the precise solution. For example, the permanent resonance frequency of a square CMUT cell with the half-side length of 93 μm and a membrane thickness of 14 μm is 4.22 MHz with the total electrical conductance of 1.96 $\mu\Omega^{-1}$, while the circular model gives the total peak conductance of 1.463 $\mu\Omega^{-1}$ at 5.01 MHz.

For further investigation, we considered two circular and square CMUTs with the same areas. For example, the area of a square CMUT with half-side length of 93 μm is equal to the area of a circular membrane with radii 105 μm. The results shown in Fig. 11 demonstrate that the total electrical conductance of a circular CMUT is more compared to a square membrane with the same area, while the resonance frequency shifts to lower values when we replace the circular membrane with a square disk with the same area.

To evaluate the effects of the CMUT physical parameters on the performance of the device and to show the accuracy of the model in detail, more circuit simulations are done in water immersion and compared with FEM. As shown in Fig. 12, three CMUTs with L/t_m of 20, 10, and 5 are considered as thin and thick membranes using the same parameters of [10, Table IV]. The simulation results of the square CMUTs are obtained for the phase and amplitude of the peak displacement and the total electrical conductance. Compared to ANSYS 3-D FEM results, circuit simulations show close predictions. However, it takes longer for FEM simulations to be completed.

Results are thus far simulated using low 1-V ac driving voltages (but with 60-V dc bias voltages close to snapdown) where small-signal models may be applicable. However, our model is also applicable to large signal operation. To demonstrate this, we performed simulations similar to those in [14], except using square, rather than circular membranes (Fig. 13). We used both FEM and our equivalent circuit model to simulate a silicon nitride membrane CMUT cell in water with

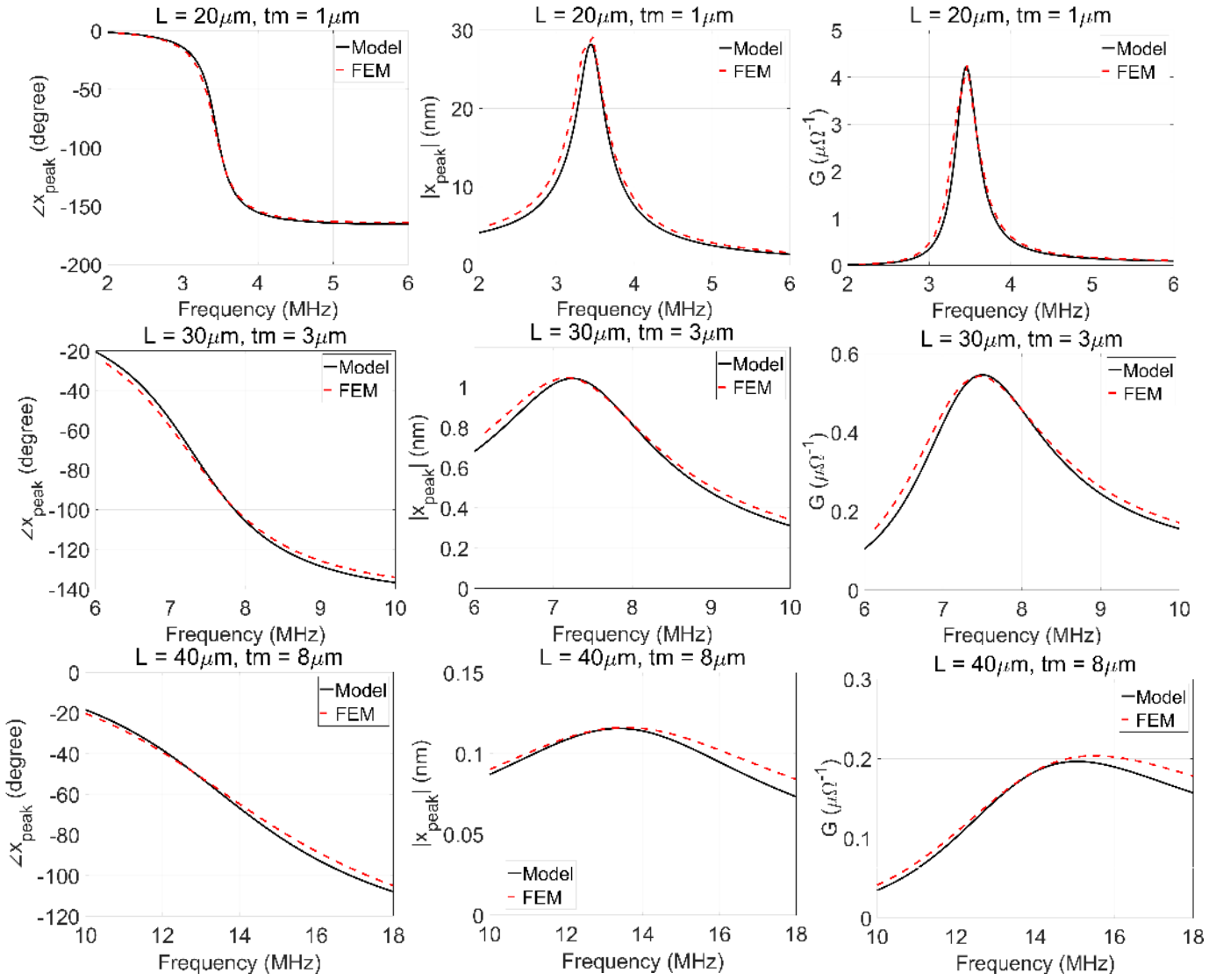

Fig. 12. Amplitude and phase of the peak displacement and the total electrical conductance of the single CMUT cells with square membranes for different L/t_m combinations. All simulations are done in water immersion for devices with parameters provided in [10, Table IV].

parameters provided in [10, Table IV]. The modeled driving voltage was 40-V peak ac, swept from 2 to 6 MHz, applied over a 10-V bias. Note that the nearly 70-nm displacement shown in Fig. 13 (top) is close to one-third of the effective gap size ($g_{\text{eff}} = 226$ nm). Because the applied voltage swings both positive and negative, this would not be a typical operating mode for CMUTs, but this simulation tests the nonlinear capacity of the model under large ac driving conditions.

IV. Fabrication

We fabricated single circular and square CMUT cells using a silicon nitride sacrificial release process that was recently developed in our group [1] with slight modifications and based on the process flow developed in [2]. Fig. 14 demonstrates the cross-sectional overview of our fabrication scheme. A prime wafer is coated with 250-nm low-stress low-pressure chemical vapor deposition (LPCVD) thin silicon nitride as insulation layer, 50-nm plasma-enhanced chemical vapor deposition (PECVD) silicon dioxide as an etch-stop layer for reactive ion etching (RIE) of the sacrificial layers and 250-nm LPCVD polysilicon sacrificial layer on it [Fig. 14(a)]. This is patterned using a highly anisotropic deep RIE (DRIE) [Fig. 14(b)] to define the area of the plugs. Then, another 100-nm LPCVD polysilicon layer is deposited [Fig. 14(c)] as the second sacrificial layer and is patterned to define the low-height etching channels while slightly increasing the polysilicon sacrificial layer in the gap area [Fig. 14(d)]. Over the patterned polysilicon sacrificial layer, 1-μm LPCVD silicon nitride is deposited as the device membrane [Fig. 14(e)].

To access the polysilicon sacrificial layer, holes are etched through the membrane [Fig. 14(f)]. Then, the membranes are released by KOH wet etching of combined sacrificial layers [Fig. 14(g)]. Long KOH etching removes the entire sacrificial layers including 350-nm polysilicon and 50-nm silicon dioxide layers beneath the gap. A low-stress PECVD silicon dioxide layer is then deposited to seal the etch holes [Fig. 14(h)], which is etched to form the sealing plugs without

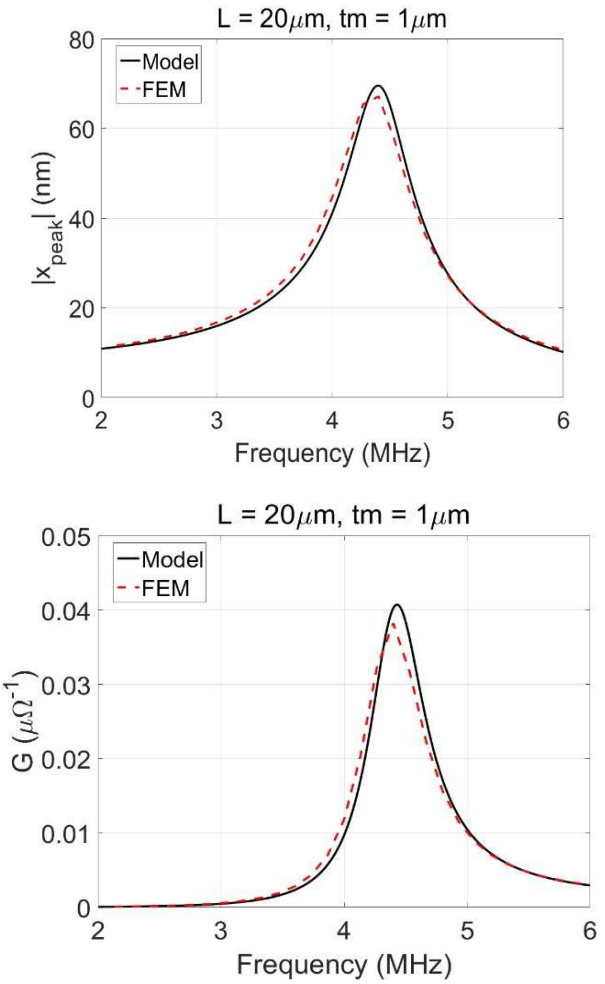

Fig. 13. Amplitude and total electrical conductance of the peak displacement of a silicon nitride membrane CMUT cell in water with parameters provided in [10, Table IV]. A 40-V peak ac signal is applied on a 10-V bias voltage. Large signal response is observed using our finite-element (FEM, dashed line) transient analysis and compared with the response of the developed equivalent circuit model shown in Fig. 1 (solid line).

TABLE III
PARAMETERS OF THE FABRICATED CMUT CELLS USING A SACRIFICIAL RELEASE PROCESS

Parameter	Values
Membrane material	Silicon Nitride
Membrane thickness, t_m (μm)	~ 1
Insulator thickness, t_i (nm)	~ 150 and 250
Gap height, t_{ga} (nm)	~ 350 - 400
Young's modulus, Y_0 (GPa)	~ 290
Density, ρ (g/cm^3)	~ 3.10
Poisson's ratio, σ	~ 0.263
Bias voltage, V_{DC} (V)	0
Driven signal, V_{AC} (V)	Pseudorandom
Medium	air Density of the air is 1.225 (kg/m^3) and speed of sound in air is 343 m/s.

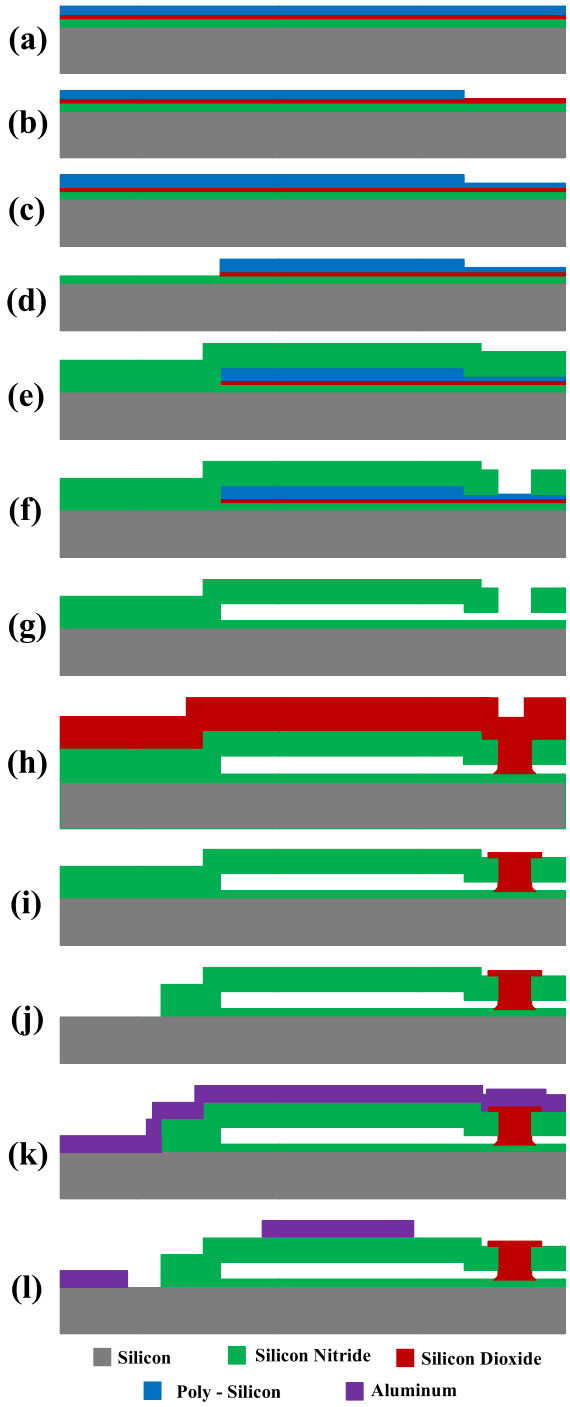

Fig. 14. Silicon nitride sacrificial release CMUT fabrication process starting on a prime wafer. (a) Deposition of thin bottom silicon nitride insulation film, silicon dioxide protection layer, and first thick polysilicon sacrificial layer. (b) Etching of the first polysilicon sacrificial layer. (c) Deposition of the second thin polysilicon sacrificial layer. (d) Etching of polysilicon sacrificial layer followed by a quick buffered oxide etch of exposed silicon dioxide protection layer. (e) Deposition of thick silicon nitride membrane. (f) Etching of the silicon nitride membrane to get access to the polysilicon sacrificial layer. (g) Chemical etching of combined sacrificial layers to release the membrane. (h) Deposition of silicon dioxide sealing film. (i) Pattering the silicon dioxide sealing film into plugs. (j) Etching through the silicon nitride film to access the bottom silicon electrode. (k) Sputtering the aluminum film. (l) Etching the aluminum layer to form the top and bottom electrodes.

coating the membranes [Fig. 14(i)]. To minimize stiction defects, the critical point drying (CPD) step must be done after releasing the membrane.

The final step after forming the CMUT cavity and sealing the holes to make the membranes is defining top and bottom electrodes. Using RIE, bottom electrode holes are etched

TABLE IV
COMPARISON OF CIRCUIT SIMULATIONS WITH EXPERIMENTAL RESULTS FOR CMUTS WITH CIRCULAR AND SQUARE MEMBRANES

CMUT	Half side length* (μm)	Resonance Frequency of Circular Single CMUT Cells		Resonance Frequency of Square Single CMUT Cells		Difference between the Resonance Frequencies of Circular and Square CMUTs using Experiments (MHz)
		Experimental Results (MHz)	Simulation Results (MHz)	Experimental Results (MHz)	Simulation Results (MHz)	
1	40	3.3312	3.263	2.9906	2.679	0.3406
2	35	4.1250	4.265	3.6844	3.515	0.4406
3	30	5.3344	5.544	4.7125	4.582	0.6219
4	25	7.3250	7.607	6.4060	6.307	0.919
5	20	11.1594	11.89	9.5875	9.908	1.5719

*The radii of the circular devices are equal to the half-side-length of the square cells.

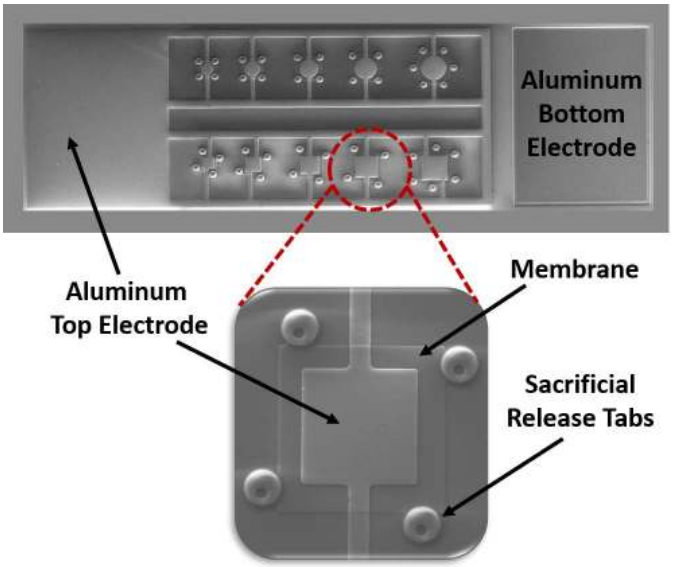

Fig. 15. SEM image of the fabricated CMUT devices with circular and square membranes using a standard sacrificial release process. The radii of the circular devices are equal to the half-side length of the counterpart square CMUTs. Top electrodes of the CMUT cells are connected and all the devices have a common bottom electrode through the silicon substrate.

through the silicon nitride layer to access the substrate which is silicon [Fig. 14(j)]. Using a magnetron sputtering system, the entire device is covered by a 400-nm aluminum layer [Fig. 14(k)], and finally, top and bottom electrodes are formed by wet aluminum etching [Fig. 14(l)]. More details about the fabrication process can be found in [1].

V. COMPARISON WITH EXPERIMENTAL RESULTS

In addition to FEA, the simulation results were validated by comparing the resonance frequencies of designed single CMUT cells with fabricated circular and square transducers using the silicon nitride sacrificial release process described above. The measurements were made using a Microsystem Analyzer laser vibrometer (MSA-500, Polytec). A pseudorandom signal, which is equally weighted in all frequencies, was applied to determine the center frequency of the devices in air. Due to the softening of the membrane, the resonance frequency of the CMUTs is shifted to lower frequencies by increasing the dc bias. To find the actual resonance frequency, we only applied pseudorandom signals without a dc bias. Fig. 15 shows the scanning electron microscopy (SEM) image of the fabricated circular and square CMUT cells with provided parameters in Table III. To compare the resonance frequency of the circular and square MUTs, the radii of the circular devices are considered to be equal to the half-side length of the square transducers. Circular CMUTs of radius 40, 35, 30, 25, and 20 μm were fabricated, tested, and compared with square CMUTs of equivalent half-side-lengths. Table IV shows an excellent agreement between the simulation and experimental results both for circular and square devices. As can be seen, the difference between the resonance frequency of the counterpart circular and square CMUTs becomes larger, as the size of the membrane gets smaller.

We applied a 1-V pseudorandom signal with different dc biases to a single square CMUT cell with the half-side length of 25 μm to find the collapse voltage and observe the changes in resonance frequency (Fig. 16). As can be seen, due to the softening of the membrane, the resonance frequency of the device is shifted to lower frequencies by increasing the dc bias. Using the HB circuit analysis, the snap-down voltage was found to be 93 and 110 V for the devices with insulator thicknesses of 150 and 250 nm, respectively. Obtained circuit simulations for the snap-down voltage match with experimental results which are around 90 and 105 V. We expected to get better agreement between simulation and experimental results when applying low voltages, but in Fig. 16, we observe better results for higher biases. This may be because of differences between the simulation parameters and the parameters of the actual fabricated devices. These differences may occur due to slight variations during the fabrication process.

VI. DISCUSSION AND CONCLUSION

A nonlinear large signal equivalent circuit model was developed for a single uncollapsed CMUT cell with square membranes. The deflection profile of a square plate was studied first, and then the nonlinear capacitance of the square CMUT was obtained using numerical analysis. The polynomial fitting was done on obtained capacitance curves for different normalized deflection areas and the first and second derivatives of the capacitances were calculated. The compliance of the membrane was calculated for thin square plates and then, by comparing the finite-element simulations and circuit model, two correction factors are obtained for thin and thick plates and then applied to the compliance. The model was designed and implemented in a circuit simulator

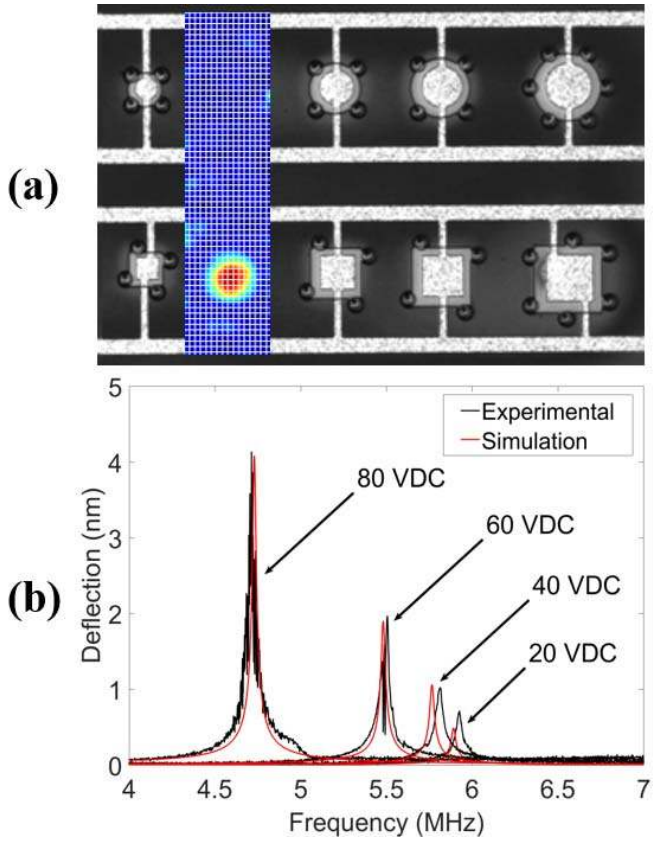

Fig. 16. Sample laser Doppler vibrometer measurements. (a) 2-D scan showing membrane displacement for 40 V_{dc} bias and 1-V pseudorandom ac signal. (b) Single point measurement using a 1-V pseudorandom ac signal with different dc biases. Peak represents the optimum resonance frequency of the device for a given dc bias and the frequency is shifted to lower frequencies by increasing the dc bias due to the softening of the membrane.

and compared with FEM and experimental results. ANSYS 3-D FEA was used to validate the equivalent circuit model predictions by performing static, prestressed harmonic, and nonlinear transient analysis. The static analysis for calculating the peak deflection of the membrane showed an excellent agreement with FEA. Moreover, the performance of the model was examined for dynamic analysis. The advanced design system (ADS) circuit model could predict many intrinsic properties of a square CMUT cell including static deflection, resonance frequency, phase and magnitude of the membrane displacement, membrane velocity, electrical conductance, and collapse voltage with accuracy comparable with FEM but within considerably less time. The results were compared with circular CMUT cells when the half-side length of the square CMUT is assumed to be equal to the radii of the circular transducer.

Single CMUT cells with silicon nitride membranes were fabricated using a standard sacrificial release process. The comparison between the ADS circuit simulations and the experimental results showed a good agreement for the resonance frequency and the membrane deflection.

Our model can include atmospheric pressure but has yet to include residual stress of the membrane. Inclusion of these residual stresses and more accurate material and device structural parameters may further improve model accuracy in future work.

Even though we used a circular membrane approximation for the acoustic self-radiation impedance, we used improved accuracy models for square membranes for other lumped circuit elements and found high accuracy when comparing both finite-element simulations and experimental results. Future work should consider the computational evaluation of the self-radiation impedance of square membranes to compare the incremental accuracy improvement over the circular membrane self-radiation impedance approximation.

The studies presented here could be used as a framework for designing the arrays with square CMUT cells. However, the effects of the mutual-acoustic impedance between the square cells of the same and different sizes should be investigated in detail and implemented into a circuit model as a z matrix to evaluate the performance of the array. Future work should aim to expand these results for improved modeling of the multifrequency CMUT arrays with square cells and their novel applications.

TABLE V
POLYNOMIAL COEFFICIENTS OF FUNCTION $g(u)$ FOR CAPACITANCE CALCULATION

$u = \frac{x_p(t)}{t_{ge}}$	$0 < u < 10^{-3}$	$10^{-3} < u < 0.5$	$0.5 < u < 0.99$
n	a_n	a_n	a_n
0	1	1	1.47200
1	0.30370	0.3037	0.21400
2	0.17990	0.1798	0.03438
3	0.03161	0.1293	-0.0244
4	426.400	0.08433	0.08047
5	-1.112e6	0.1801	0.08518
6	1.759e9	-0.3259	-0.05122
7	-1.657e12	1.0070	-0.04796
8	8.547e14	-1.2320	0.01346
9	-1.859e17	0.8414	0.01037
$(Goodness\ of\ fit)$			
SSE	4.187e-26	1.509e-11	5.058e-3
R-square	1	1	0.9999
Adjusted R-square	1	1	0.9999
RMSE	2.047e-15	5.504e-8	3.277e-3

APPENDIX

The polynomial coefficients of (7) for different normalized deflection areas of $x_p(t)/t_{ge}$ are computed using a polynomial curve fitting method to give a best fit to numerical solutions of (5) and are shown in Table V.

ACKNOWLEDGMENT

The authors would like to thank CMC Microsystems for the provision of products and services that facilitated this paper including CAD software packages. They would also like to thank Prof. A. Atalar of Bilkent University as well as Dr. H. K. Oğuz of Siemens Healthineers for assistance with ADS and ANSYS modeling.

REFERENCES

[1] B. A. Greenlay and R. J. Zemp, "Fabrication of linear array and top-orthogonal-to-bottom electrode CMUT arrays with a sacrificial release process," *IEEE Trans. Ultrason., Ferroelectr., Freq. Control*, vol. 64, no. 1, pp. 93–107, Jan. 2017.

[2] A. S. Erguri, Y. Huang, X. Zhuang, Ö. Oralkan, G. G. Yarahoglu, and B. T. Khuri-Yakub, "Capacitive micromachined ultrasonic transducers: Fabrication technology," *IEEE Trans. Ultrason., Ferroelectr., Freq. Control*, vol. 52, no. 12, pp. 2242–2258, Dec. 2005.

[3] B. T. Khuri-Yakub and Ö. Oralkan, "Capacitive micromachined ultrasonic transducers for medical imaging and therapy," *J. Micromech. Microeng.*, vol. 21, no. 5, Apr. 2011, Art. no. 054004.

[4] P. Zhang, G. Fitzpatrick, T. Harrison, W. A. Moussa, and R. J. Zemp, "Double-SOI wafer-bonded CMUTs with improved electrical safety and minimal roughness of dielectric and electrode surfaces," *J. Microelectromech. Syst.*, vol. 21, no. 3, pp. 668–680, Jun. 2012.

[5] M. Maadi and B. Bayram, "Custom integrated circuit design for ultrasonic therapeutic CMUT array," *Microsyst. Technol.*, vol. 21, no. 4, pp. 875–891, Apr. 2015.

[6] M. Maadi, C. Ceroici, and R. J. Zemp, "Electrical impedace matching of CMUT cells," in *Proc. IEEE Int. Ultrason. Symp.*, Taipei, Taiwan, Oct. 2015, pp. 1–4.

[7] A. Sampaleanu, P. Zhang, A. Kshirsagar, W. Moussa, and R. J. Zemp, "Top-orthogonal-to-bottom-electrode (TOBE) CMUT arrays for 3-D ultrasound imaging," *IEEE Trans. Ultrason., Ferroelectr., Freq. Control*, vol. 61, no. 2, pp. 266–276, Feb. 2014.

[8] A. Kshirsagar *et al.*, "Multi-frequency CMUT arrays for imaging-therapy applications," in *Proc. IEEE Int. Ultrason. Symp. (IUS)*, Jul. 2013, pp. 1991–1993.

[9] M. Maadi, R. Chee, and R. J. Zemp, "Mutual radiation impedance for modeling of multi-frequency CMUT arrays," in *Proc. IEEE Int. Ultrason. Symp. (IUS)*, Taipei, Taiwan, Oct. 2015, pp. 1–4.

[10] M. Maadi and R. J. Zemp, "Self and mutual radiation impedances for modeling of multi-frequency CMUT arrays," *IEEE Trans. Ultrason., Ferroelectr., Freq. Control*, vol. 63, no. 9, pp. 1441–1454, Sep. 2016.

[11] M. Maadi and R. J. Zemp, "Modelling of large-scale multi-frequency CMUT arrays with circular membranes," in *Proc. IEEE Int. Ultrason. Symp. (IUS)*, Tours, France, Sep. 2016, pp. 1–4.

[12] R. K. W. Chee, P. Zhang, M. Maadi, and R. J. Zemp, "Multifrequency interlaced CMUTs for photoacoustic imaging," *IEEE Trans. Ultrason., Ferroelectr., Freq. Control*, vol. 64, no. 2, pp. 391–401, Feb. 2017.

[13] W. P. Mason, *Electromechanical Transducers and Wave Filters*, 2nd ed. New York, NY, USA: Van Nostrand, 1948.

[14] H. Köymen *et al.*, "An improved lumped element nonlinear circuit model for a circular CMUT cell," *IEEE Trans. Ultrason., Ferroelectr., Freq. Control*, vol. 59, no. 8, pp. 1791–1799, Aug. 2012.

[15] H. K. Oguz, S. Olcum, M. N. Senlik, V. Tas, A. Atalar, and H. Köymen, "Nonlinear modeling of an immersed transmitting capacitive micromachined ultrasonic transducer for harmonic balance analysis," *IEEE Trans. Ultrason., Ferroelectr., Freq. Control*, vol. 57, no. 2, pp. 438–447, Feb. 2010.

[16] H. Köymen, M. N. Senlik, A. Atalar, and S. Olcum, "Parametric linear modeling of circular cMUT membranes in vacuum," *IEEE Trans. Ultrason., Ferroelectr., Freq. Control*, vol. 54, no. 6, pp. 1229–1239, Jun. 2007.

[17] M. F. la Cour, T. L. Christiansen, J. A. Jensen, and E. V. Thomsen, "Electrostatic and small-signal analysis of CMUTs with circular and square anisotropic plates," *IEEE Trans. Ultrason., Ferroelectr., Freq. Control*, vol. 62, no. 8, pp. 1563–1579, Aug. 2015.

[18] E. V. Thomsen, K. Reck, G. Skands, C. Bertelsen, and O. Hansen, "Silicon as an anisotropic mechanical material: Deflection of thin crystalline plates," *Sens. Actuators A, Phys.*, vol. 220, pp. 347–364, Dec. 2014.

[19] F. C. Mbakogu and M. N. Pavlović, "Bending of clamped orthotropic rectangular plates: A variational symbolic solution," *Comput. Struct.*, vol. 77, no. 2, pp. 117–128, Jun. 2000.

[20] M. Rahman, J. Hernandez, and S. Chowdhury, "An improved analytical method to design CMUTs with square diaphragms," *IEEE Trans. Ultrason., Ferroelectr., Freq. Control*, vol. 60, no. 4, pp. 834–845, Apr. 2013.

[21] Z. Zheng, W. Sun, X. Suo, L. L. P. Wong, Z. Sun, and J. T. W. Yeow, "A novel deflection shape function for rectangular capacitive micromachined ultrasonic transducer diaphragms," *Sens. Bio-Sens. Res.*, vol. 5, pp. 62–70, Sep. 2015.

[22] S. Satir, J. Zahorian, and F. L. Degertekin, "A large-signal model for CMUT arrays with arbitrary membrane geometry operating in non-collapsed mode," *IEEE Trans. Ultrason., Ferroelectr., Freq. Control*, vol. 60, no. 11, pp. 2426–2439, Nov. 2013.

[23] J. Zahorian, S. Satir, and F. L. Degertekin, "Analytical-finite element hybrid model for CMUT arrays with arbitrary membrane geometry," in *Proc. IEEE Int. Ultrason. Symp. (IUS)*, Dresden, Germany, Oct. 2012, pp. 584–587.

[24] F. Y. Yamaner, S. Olcum, H. K. Oguz, A. Bozkurt, H. Köymen, and A. Atalar, "High-power CMUTs: Design and experimental verification," *IEEE Trans. Ultrason., Ferroelectr., Freq. Control*, vol. 59, no. 6, pp. 1276–1284, Jun. 2012.

[25] M. N. Senlik, S. Olcum, H. Köymen, and A. Atalar, "Radiation impedance of an array of circular capacitive micromachined ultrasonic transducers," *IEEE Trans. Ultrason., Ferroelectr., Freq. Control*, vol. 57, no. 4, pp. 969–976, Apr. 2010.

[26] H. K. Oguz, "Circuit theory based modeling and analysis of CMUT arrays," Ph.D. dissertation, Dept. Elect. Electron. Eng., Bilkent Univ., Ankara, Turkey, 2013.

Mohammad Maadi (S'15) was born in Macoo, Western Azarbaijan, Iran, in 1985. He received the M.S. degree in electrical and electronics engineering from Middle East Technical University (METU), Ankara, Turkey, in 2013. He is currently pursuing the Ph.D. degree with the Electrical and Computer Engineering Department, University of Alberta, Edmonton, AB, Canada.

From 2011 to 2013, he was a Research Assistant with METU, where he was involved in the integrated circuit design for capacitive micromachined ultrasonic transducers (CMUTs). He is currently a Research and Teaching Assistant with the University of Alberta. His current research interests include the design, fabrication, and characterization of large-scale multifrequency CMUT arrays with associated electronics for ultrasound medical imaging applications.

Mr. Maadi is a member of the Golden Key International Society, the world's largest collegiate honor society. He was a recipient of the Alberta Innovates Technology Futures Graduate Student Scholarship in 2016.

Roger J. Zemp (S'04–M'04) was born in Calgary, AB, Canada, in 1974. He received the B.Sc. degree in physics from the University of Alberta, Edmonton, AB, Canada, in 1998, the M.A.Sc. degree in electrical and computer engineering from the University of Toronto, Toronto, ON, Canada, in 2000, and the Ph.D. degree in biomedical engineering from the University of California at Davis, Davis, CA, USA, in 2004.

From 2004 to 2006, he was a Post-Doctoral Fellow at Texas A&M University. From 2006 to 2007, he was with Washington University, St. Louis, MO, USA. He is currently a Full Professor with the Department of Electrical and Computer Engineering, University of Alberta. His research interests include ultrasound imaging, biomedical optics, and photoacoustic imaging.

Dr. Zemp has been an Associate Editor of the IEEE TRANSACTIONS ON ULTRASONICS, FERROELECTRICS, AND FREQUENCY CONTROL since 2013.